CAAP Quarterly Report

[06/30/2024]

***Project Name**: Multi-Compound Green Corrosion Inhibitor for Gas Pipeline: Synthesis, Optimization, and Evaluation*

***Contract Number**: 693JK32350004CAAP*

***Prime University**: Arizona State University*

***Prepared By**: Dr. Yongming Liu (PI), Dr. Shuguang Deng (Co-PI), Dr. Tekle Fida (Co-PI), Xuandong Lu, Adi Venkata Sandeep Yalamanchili, Mohammadjavad Kazemi, Sai Niranjan*

***Reporting Period**: [4/2025 – 6/2025]*

Project Activities for Reporting Period:

Task 1. Design and Synthesis of Multi-compound Green Inhibitors

The team focused on developing and optimizing fatty acid-based green inhibitors derived from a variety of natural oil sources. The primary goal was to modify these fatty acids to enhance their corrosion inhibition efficiency. Specifically, the modifications aimed at transforming the fatty acids into water-soluble, surfactant-like inhibitors, thereby improving their dispersibility and enhancing their interactions with metal surfaces. By evaluating the corrosion inhibition performance of these modified fatty acid mixtures in comparison to a control sample, the study seeks to provide a deeper understanding of their relative effectiveness. Additionally, the research delves into the corrosion inhibition mechanisms of both unmodified (free) fatty acids and their surfactant-modified analogs, identifying similarities and differences in their modes of action. The ultimate objective is to generate valuable insights that will inform the design and development of more efficient, sustainable, and environmentally friendly corrosion inhibitors.

Task 1.2: Synthesis and Characterization of Green Inhibitors from Renewable Feedstock

- Synthesizing mixtures of free fatty acids through the hydrolysis of various bio-oils to serve as corrosion inhibitors.
- Enhancing the corrosion inhibition efficiency of the produced inhibitors by incorporating polyethylene glycol to improve their performance.
- Submitting an invention disclosure titled "Sustainable Water-Soluble Corrosion Inhibitor from Waste Cooking Oil via Fatty Acid Ethoxylation" to Arizona State University.

Task 2. Simulation-based Inhibitor Optimization in Gas Gathering and Transportation Pipelines

During this reporting period, we have made significant progress in Task 2, focusing on identifying high-risk corrosion locations in gas pipelines based on Internal Corrosion Direct Assessment (ICDA) and applying the AI-enhanced approach for more efficient prediction on short-distance inhibitor deposition with optimizing atomizer settings. The key activities are outlined below:

Task 2.2: AI-assisted inhibitor optimization gathering and transportation pipelines

- Established a framework for identifying high-risk locations and reinforcing corrosion prevention through targeted inhibitor injection.
- Identified high-risk corrosion locations based on ICDA.
- Investigated the effect of computational fluid dynamics (CFD) parameters on particle transport.
- Optimized atomizer setting with an injection Control Network (ICN).

Planned Project Work in the next quarter:

For Task 1:

- Establishing the absorption isotherm of fatty acid-based inhibitors
- Modifying pectin as another selected candidate in task 1.1

For Task 2:

- Continue investigation of the inhibitor implementation optimization using AI-assisted tools

For Task 3:

- Investigate a suitable measurement method, such as optical and electrochemical methods, to assess inhibitor distribution and degradation;
- Establish a multi-factor safety index model and design a simple tool for practical corrosion risk assessment in the field.

Project Financial Activities Incurred during the Reporting Period:

For Task 1, we supported 1 RA at ASU
For Tasks 2-3, we supported 1 RAs at ASU

Project Activities with Cost Share Partners:

Engaged in discussions with the Technical Advisory Panel members to solicit recommendations for our team's research activities.

Project Activities with External Partners:

Conducted regular discussions with the Technical Advisory Panel, in addition to several separate meetings and email communications with individual advisory members.

Potential Project Risks:

Nothing to report.

Appendix 1
Technical Progress Description for Task 1

Task 1. Design and Synthesis of Multi-compound Green Inhibitors

1. Introduction

Free fatty acids (FFAs) act as effective corrosion inhibitors by adsorbing onto metal surfaces, forming a protective barrier that limits the penetration of corrosive agents. These amphiphilic molecules possess a polar hydrophilic head (the carboxylic acid group, –COOH) and a nonpolar hydrophobic tail (a long hydrocarbon chain). The –COOH group strongly binds to metal surfaces, particularly steel, by interacting with Fe^{2+} or Fe^{3+} ions through chemisorption, ensuring a stable attachment to the metal. Once adsorbed, the hydrophobic tail extends into the aqueous environment, forming a dense monolayer that blocks the ingress of water, oxygen, and aggressive ions like chlorides. This dual functionality—anchoring to the metal via the head group and protecting the surface with the tail—enables FFAs to effectively inhibit corrosion in both neutral and acidic conditions.

The corrosion inhibition efficiency of FFAs is largely influenced by their chemical structure, particularly the degree of saturation in their hydrocarbon chains. Saturated fatty acids, such as stearic acid (C18:0) and palmitic acid (C16:0), consist entirely of single carbon-carbon bonds. These acids are more thermally and chemically stable but tend to be less reactive. On the other hand, unsaturated fatty acids, such as oleic acid (C18:1) and linoleic acid (C18:2), contain one or more double bonds that create bends in their molecular structure. While these bends may reduce the packing density of the monolayer, they can also enhance flexibility and surface interaction, which may improve corrosion protection.

Furthermore, FFAs differ notably from their soap derivatives. In soaps, the –COOH group is converted into a carboxylate salt ($–COO^-$) when it reacts with a strong base like NaOH, increasing solubility and interaction with water. In contrast, FFAs largely remain non-ionized at neutral pH, making them less soluble in water. While this affects their transport and adsorption properties, it allows them to form hydrophobic, water-resistant films on metal surfaces, further enhancing their corrosion inhibition potential.

2. Methodology

2.1 Materials

Soybean oil, canola oil, sunflower oil, olive oil, and castor oil were sourced from local suppliers and used as renewable feedstocks without additional purification. Polyethylene glycol (PEG-400, with an average molecular weight of approximately 400 g/mol) and concentrated sulfuric acid (H_2SO_4, ≥98%) were purchased from Sigma-Aldrich. Hydrochloric acid (HCl, 37%) was diluted with deionized water to prepare 1 M HCl solutions for corrosion testing. Analytical-grade oleic acid was utilized directly as a model free fatty acid inhibitor for both comparison and modification purposes. All chemicals used were of analytical reagent grade. A36 carbon steel coupons, measuring 0.5 inches by 1.0 inch, served as the working electrodes in all corrosion experiments. Prior to immersion, the prepared coupons were carefully weighed using an analytical balance with a precision of ±0.1 mg.

2.2 Synthesis of Free Fatty Acids Mixtures from Bio-Oils

To extract free fatty acids from the selected bio-oils, a non-catalytic hydrolysis method was employed. Equal volumes (1:1 v/v) of each oil and deionized water were combined in a sealed stainless-steel autoclave reactor. The mixture was heated to 250°C and held at this temperature for 30 minutes to facilitate thermal hydrolysis. After the reaction, the system was cooled to room temperature, resulting in phase separation. The upper aqueous phase was discarded, while the organic phase containing the free fatty acids was carefully collected and dried under vacuum to remove any residual moisture. No solvents or neutralizing agents were used in the process, preserving the green synthesis approach.

2.3 Synthesis of Fatty Acid Methyl Esters (FAME)

Fatty acid methyl esters (FAME) were synthesized via base-catalyzed transesterification of soybean oil and subsequently used as corrosion inhibitors. A molar ratio of 6:1 (methanol: triglyceride) was employed to ensure reaction completion. Based on the average molar mass of soybean oil (approximately 929 g/mol), 50 g of oil required approximately 14.85 g of methanol to maintain the 6:1 ratio.

First, 1 g of potassium hydroxide (KOH) was weighed and dissolved in 14.85 g of methanol in a clean Erlenmeyer flask under continuous stirring. This formed a homogeneous methoxide solution. Separately, 50 g of soybean oil was weighed and added to the methoxide solution. The reaction flask was immediately sealed with aluminium foil to minimize methanol evaporation and stirred at 60 °C for 60 minutes.

Upon completion of the reaction, the mixture was allowed to settle. Due to phase separation, the denser glycerol formed the lower layer, while biodiesel (FAME) formed the upper layer. The upper FAME-rich phase was carefully decanted.

To purify the FAME, two post-treatment steps were performed:

- **Flash Evaporation**: The decanted biodiesel was briefly heated to evaporate any residual methanol.
- **Water Washing**: The FAME was washed with deionized water to remove remaining methanol and catalyst residues. The aqueous phase was separated after each wash.

The purified fatty acid methyl esters were dried and stored in an airtight container at room temperature prior to use in corrosion inhibition experiments.

2.4 Synthesis of PEG-Modified Fatty Acids (Surfactant-Type Inhibitors)

The extracted fatty acids were chemically modified via esterification with PEG-400 to improve their solubility, stability, and interaction with metal surfaces. In a typical reaction, the fatty acid and PEG-400 were mixed in a molar ratio of 1.2:1 (fatty acid:PEG) and stirred continuously under a nitrogen atmosphere to prevent oxidative degradation. Sulfuric acid (2 wt% of the total mixture) was added as a catalyst to promote ester bond formation. The reaction was carried out at 110 °C for 5 hours in a three-neck round-bottom flask equipped with a reflux condenser, nitrogen inlet, and temperature control. The final product (a viscous, surfactant-like ester) was cooled to ambient temperature and stored in airtight glass containers for further testing.

2.5 Corrosion Testing

Corrosion inhibition performance was evaluated using three methods: weight loss measurements, Tafel polarization, and electrochemical impedance spectroscopy (EIS). All experiments were conducted at room temperature (25 ± 1 °C) using 1 M HCl solution as the corrosive medium.

2.5.1 Electrochemical Corrosion Testing

For corrosion testing and validation, the inhibitors were subjected to thorough testing in hydrochloric acid (HCl). The testing framework included electrochemical impedance spectroscopy (EIS), Tafel polarization, static weight loss measurements, EIS and Tafel polarization provided essential insights into the electrochemical behavior of the inhibitors, particularly their ability to reduce corrosion currents and enhance charge transfer resistance. Static weight loss tests measured the mass loss of carbon steel samples over time, offering a direct indication of the inhibitors' efficiency in mitigating corrosion under HCL media. The selected 10 inhibitors were tested.

2.5.2 Electrochemical Impedance Spectroscopy (EIS)

The interpretation of EIS data is typically facilitated using Nyquist and Bode plots, which graphically represent the impedance characteristics of the system. These plots can reveal:

- **Charge Transfer Resistance**: Related to the ease with which electrons can move across the electrode/electrolyte interface.
- **Double Layer Capacitance**: Reflects the capacitive behavior at the interface, influenced by the thickness and properties of the electrochemical double layer.
- **Warburg Impedance**: Indicates diffusion-controlled processes, often seen in porous coatings or corrosion layers.

Electrochemical Impedance Spectroscopy (EIS) tests were conducted to evaluate the efficiency of the shortlisted corrosion inhibitors. These tests were performed in ten different media:

- Medium 1: 1 M HCl only (Control)
- Medium 2: 1 M HCl + Free fatty acids from castor oil (Castor oil)
- Medium 3: 1 M HCl + Free fatty acids from olive oil (Olive oil)
- Medium 4: 1 M HCl + Free fatty acids from soybean oil (Soybean oil)
- Medium 5: 1 M HCl + Free fatty acids from canola oil (Canola oil)
- Medium 6: 1 M HCl + Free fatty acids from sunflower oil (Sunflower oil)

- Medium 7: 1 M HCl + Fatty acid methyl ester (Fatty acid methyl ester)
- Medium 8: 1 M HCl + Commercial Oleic Acid (Oleic acid)
- Medium 9: 1 M HCl + PEG-modified castor oil fatty acids (PEG-Castor oil)
- Medium 10: 1 M HCl + PEG-modified olive oil fatty acids (PEG-Olive oil)
- Medium 11: 1 M HCl + PEG-modified soybean oil fatty acids (PEG-Soybean oil)
- Medium 12: 1 M HCl + PEG-modified canola oil fatty acids (PEG-Canola oil)
- Medium 13: 1 M HCl + PEG-modified fatty acid methyl ester (PEG-Fatty acid methyl ester)
- Medium 14: 1 M HCl + PEG-modified oleic acid (PEG-Oleic acid)
- The EIS measurements utilized a standard three-electrode cell setup:
- **Working Electrode**: c steel specimen polished and brushed using sandpaper to remove oxidable layer.
- **Reference Electrode**: Saturated calomel electrode (SCE).
- **Counter Electrode**: Platinum wire.

The Electrochemical impedance spectroscopy was performed utilizing a frequency response analyzer in conjunction with a potentiostat. This setup ensured precise maintenance of the electrode potential while recording the impedance response. A summary of the specific parameters employed during the EIS tests is presented in Table 1.1.

Table 1.1 EIS Test Parameters

Parameter	Value	Description
AC Signal Amplitude	10 mV	The amplitude of the alternating current signal.
Frequency Range	100 kHz to 10 mHz	The range over which impedance was measured.
Potentiostat Mode	Potentiostatic (constant potential)	Maintains a constant electrode potential during measurements.
Equilibration Time	At least 3 hours	Allows the system to stabilize before measurements.

EIS measurements commenced following a stabilization period, allowing the electrochemical system to achieve a steady state. Impedance data were collected over the designated frequency range to encompass the full electrochemical response.

The impedance data were analyzed by fitting them to an equivalent circuit model to extract key parameters such as solution resistance (Rs), charge transfer resistance (Rct), and constant phase element (CPE). These parameters were derived from Nyquist plots, which graph the imaginary part of impedance (Z'') against the real part (Z').

The equivalent circuit used for analyzing the impedance plots consisted of:

- **R1**: Solution resistance (Rs).
- **R2**: Charge transfer resistance (Rct).
- **CPE1**: Impedance of the constant phase element.

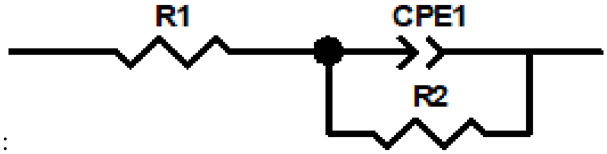

:

Figure 1.1. Equivalent Circuit Used for Analyzing the Impedance Spectra

Steps for Measuring Solution and Charge Transfer Resistance

- **Perform EIS Measurement**: Conduct an EIS experiment over a broad frequency range.
- **Analyse Nyquist Plot**: Plot the Nyquist diagram and identify the intercepts and features corresponding to Rs and Rct.
- **Calculation of Parameters**:
- **Solution Resistance (Rs)**: High-frequency intercept on the real axis of a Nyquist plot.
- **Charge Transfer Resistance (Rct)**: Represents the electron transfer resistance at the electrode-electrolyte interface.

2.5.3 Tafel Polarization

Equipment Setup and Preparation

For the Tafel polarization test, a controlled electrochemical setup was utilized, typically comprising a potentiostat, a three-electrode cell, and software for data acquisition and analysis. The three-electrode system consisted of a working electrode (the metal under test), a reference electrode, and a counter electrode.

Stabilization of Open Circuit Potential (OCP)

The metal sample was immersed in the test solution, and the system was allowed to equilibrate to the open circuit potential (OCP). This step was crucial as it established a stable baseline condition, for the electrochemical system. The OCP is the potential where the net current at the electrode surface is zero, indicating that the rates of the anodic and cathodic reactions have reached equilibrium.

Test Parameter Configuration

The configuration of the test parameters was performed through the software interface of the potentiostat. Key parameters entered included:

- **Initial Potential (Einitial)**: Set 10 mV negative relative to the OCP. This was the starting point for the potential sweep.
- **Final Potential (Efinal)**: Set 10 mV positive relative to the OCP. This defined the endpoint of the potential sweep.

- **Scan Rate**: Determined to be approximately 0.125 mV/s. The scan rate was crucial for ensuring that the system did not deviate significantly from equilibrium during the test.

Execution of the Potentiodynamic Polarization Tests

Once the parameters were set, the potentiodynamic polarization test was initiated. The software controlled the potentiostat to apply a linear sweep of potential from the initial to the final set values. During this sweep:

- The potential was incrementally increased from Einitial to Efinal.
- The current response of the system was continuously measured as the potential was varied.

Data Acquisition and Plotting

The current and potential data collected during the tests were automatically recorded by the software. This data was used to generate the Tafel plot, which graphed the potential (E) on the Y- axis versus the logarithm of the current density (log I) on the X-axis. The Tafel plot was essential for analyzing the electrochemical behavior of the metal under the test conditions

Identification of Linear Regions and Extrapolation

The Tafel plot typically exhibited linear regions corresponding to the anodic and cathodic branches. These regions were critical for the analysis as they reflected the kinetics of the oxidation and reduction reactions. Using the software:

- The linear portions of the anodic and cathodic curves were identified.
- These linear regions were extrapolated back to their intersection at the corrosion potential (Ecorr).

Calculation of Corrosion Current Density (i_{corr})

The intersection points of the extrapolated anodic and cathodic lines provided the corrosion current density (icorr), which is a critical parameter directly related to the corrosion rate of the metal. Using specialized software, icorr was converted into the corrosion rate by applying predefined constants and material properties, such as the metal's equivalent weight (EW) and density. Subsequently, the corrosion rate (CR) of the corrosion inhibitor were calculated using the following formulas:

$$\mathrm{CR} = \frac{\mathrm{I_{corr} K\,EW}}{\rho \mathrm{A}} \tag{1}$$

- Medium 1: 1 M HCl only (Control)
- Medium 2: 1 M HCl + Free fatty acids from castor oil (Castor oil)
- Medium 3: 1 M HCl + Free fatty acids from olive oil (Olive oil)
- Medium 4: 1 M HCl + Free fatty acids from soybean oil (Soybean oil)
- Medium 5: 1 M HCl + Free fatty acids from canola oil (Canola oil)
- Medium 6: 1 M HCl + Free fatty acids from sunflower oil (Sunflower oil)
- Medium 7: 1 M HCl + Fatty acid methyl ester (Fatty acid methyl ester)

- Medium 8: 1 M HCl + Commercial Oleic Acid (Oleic acid)
- Medium 9: 1 M HCl + PEG-modified castor oil fatty acids (PEG-Castor oil)
- Medium 10: 1 M HCl + PEG-modified olive oil fatty acids (PEG-Olive oil)
- Medium 11: 1 M HCl + PEG-modified soybean oil fatty acids (PEG-Soybean oil)
- Medium 12: 1 M HCl + PEG-modified canola oil fatty acids (PEG-Canola oil)
- Medium 13: 1 M HCl + PEG-modified fatty acid methyl ester (PEG-Fatty acid methyl ester)
- Medium 14: 1 M HCl + PEG-modified oleic acid (PEG-Oleic acid)

2.6 Static Weight Loss in 1M HCl

The experiments were conducted over the course of one week to evaluate the corrosion behavior of various inhibitors. To minimize oxygen exposure and maintain consistent environmental conditions, all test beakers were placed inside a fume hood. Prior to immersion, each A36 carbon steel coupon was carefully weighed to record its initial mass with high precision. Following the exposure period, the coupons were retrieved and cleaned to remove any corrosion products. Cleaning involved scrubbing under running water using a bristle brush, followed by rinsing with acetone. The cleaned coupons were then dried in acetone to eliminate residual moisture before being reweighed to determine their final mass.

Corrosion was quantified by weight loss, calculated as the difference between the initial and final mass. This metric enabled a direct comparison of the protective effectiveness of the tested inhibitors, which included free and PEG-modified fatty acids derived from soybean, canola, sunflower, olive, and castor oils, as well as fatty acid methyl esters and commercial oleic acid in both unmodified and PEG-modified forms. A harsh testing environment, 1 M hydrochloric acid (HCl), was used to simulate aggressive corrosion conditions and identify the most effective inhibitors under extreme scenarios.

3. Result and Analysis

3.1 Electrochemical Corrosion Testing

3.1.1 Electrochemical Impedance Spectroscopy (EIS)

Electrochemical Impedance Spectroscopy (EIS) was employed to evaluate the corrosion inhibition performance of unmodified and PEG-modified fatty acid-based inhibitors in 1 M HCl. The key parameters extracted from the EIS spectra include solution resistance (Rs), polarization resistance (Rp), constant phase element (CPE), and the phase shift factor (n), with inhibition efficiency calculated from Rp values. A higher Rp value correlates directly with enhanced corrosion protection, as it reflects the ability of the inhibitor to hinder charge transfer processes at the metal–electrolyte interface.

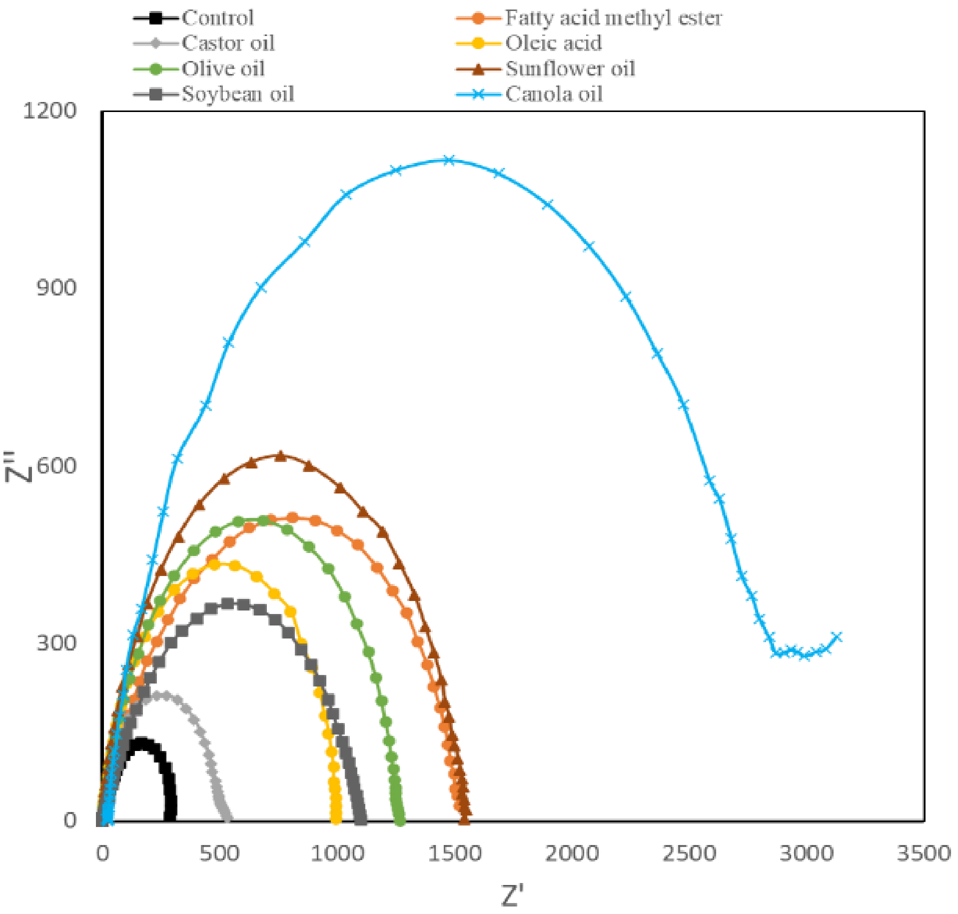
Control
Fatty acid methyl ester
Castor oil
Oleic acid
Olive oil
Sunflower oil
Soybean oil
Canola oil
1200
900
600
300
0
Z''
0
500
1000
1500
2000
2500
3000
3500
Z'

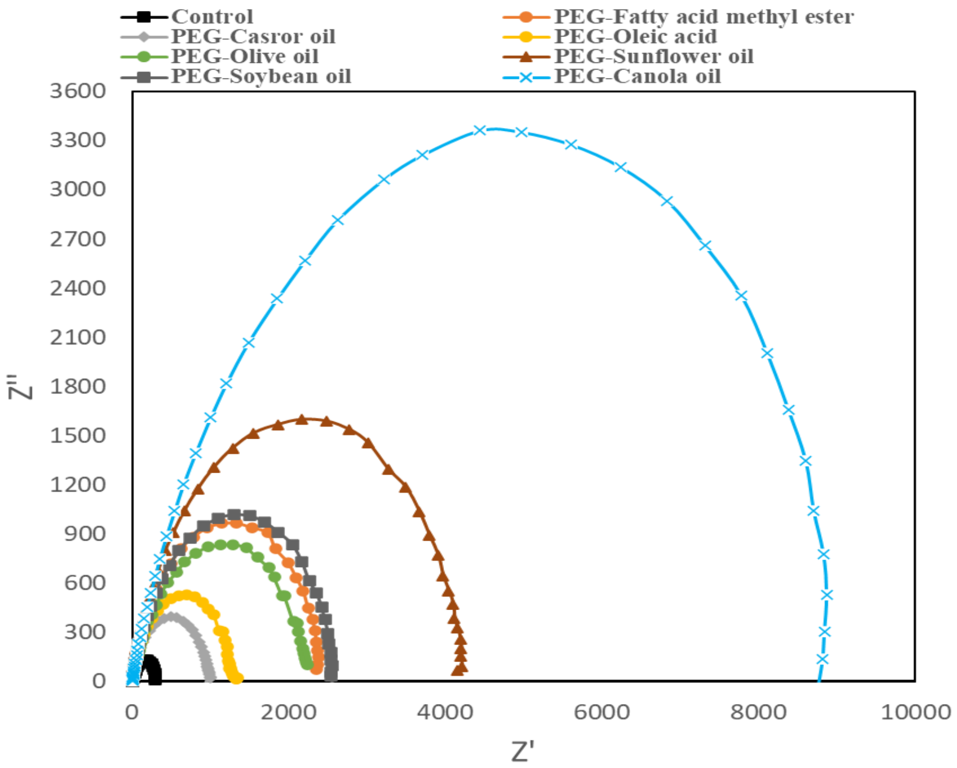

Figure 1.2. EIS plots of unmodified (up) and modified free fatty acid mixes (down)

Table 1.2. EIS test results of unmodified free fatty acid mixes in 1M HCL and associated inhibition efficiency results of unmodified and associated inhibition efficiency

Sample	Rs (solution resistance) (Ω cm^2)	RP (Polarization resistance) (Ω cm^2)	CPE (constant phase element) (F/s)	n	Inhibition efficiency (%)
Control	1.232	298.6	8.8 * 10-4	0.838	-------
Canola oil	21.500	2889.3	1.43 * 10-5	0.860	89.66
Castor oil	0.926	473.6	3.35 * 10-5	0.949	36.95
Sunflower oil	0.77	1545	5.44 * 10-5	0.855	80.67
Olive oil	1.313	1258	3.85 * 10-5	0.851	76.3
Soybean oil	0.680	1163	7.89 * 10-5	0.664	74.3
Oleic Acid	1.123	967.9	5.9 * 10-5	0.894	69.1
Fatty acid methyl ester	1.217	1548	3.16 * 10-5	0.744	80.71

Table 1.3. EIS test results of modified free fatty acid mixes in 1M HCL and associated inhibition efficiency results of unmodified and associated inhibition efficiency

Sample	Rs (solution resistance) (Ω cm^2)	RP (Polarization resistance) (Ω cm^2)	CPE (constant phase element) (F/s)	n	Inhibition efficiency (%)
Control	1.232	298.6	8.8 * 10-4	0.838	-------
Canola oil	2.1	9169	3.35 * 10-6	0.789	96.74
Castor oil	1.173	989.6	8.2 * 10-5	0.812	69.8
Sunflower oil	1.124	3932	1.54 * 10-5	0.865	92.4
Olive oil	1.046	2197	1.8 * 10-5	0.835	86.4
Soybean oil	1.318	2591	2.27 * 10-5	0.823	88.48
Oleic Acid	0.9898	1189	2.9 * 10-5	0.898	74.9
Fatty acid methyl ester	0.9562	2095	1.9 * 10-5	0.900	85.5

For the unmodified inhibitors (Table 1.2), the control sample exhibited a baseline Rp of 298.6 Ω·cm², with all inhibitors showing substantial improvements. Canola oil achieved the highest Rp of 2889.3 Ω·cm², corresponding to an inhibition efficiency of 89.66%. FAME and sunflower oil showed comparable performances with efficiencies of 80.71% and 80.67%, respectively. Olive oil and soybean oil exhibited inhibition efficiencies of 76.3% and 74.3%, while castor oil performed significantly lower at 36.95%. Oleic acid showed moderate effectiveness with 69.1% inhibition. These results align with trends observed in the Tafel data, confirming the relatively high effectiveness of fatty acid mixtures from canola, sunflower, and soybean oils in reducing corrosion.

Upon PEG modification (Table 1.3), all systems demonstrated marked improvements in Rp and inhibition efficiency. Canola oil showed the most substantial increase, with Rp rising from 2889.3 Ω·cm² to 9169 Ω·cm², boosting its inhibition efficiency from 89.66% to 96.74% (+7.08 percentage points). Similarly, sunflower oil improved from 80.67% to 92.4% (+11.73 points), and soybean oil from 74.3% to 88.48% (+14.18 points). Olive oil increased from 76.3% to 86.4% (+10.1 points), and oleic acid showed improvement from 69.1% to 74.9% (+5.8 points). FAME also exhibited enhanced performance, with inhibition efficiency increasing from 80.71% to 85.5% (+4.79 points). Notably, even castor oil, which initially had low performance, improved from 36.95% to 69.8%, a substantial 32.85-point increase, indicating the significant benefit of PEG functionalization in cases with initially poor inhibition.

These findings confirm that PEG modification consistently increases the effectiveness of fatty acid-based inhibitors by improving their adsorption characteristics, forming more compact and protective interfacial films, and enhancing the resistance to charge transfer, as reflected in the increased Rp values.

3.1.2 Tafel Polarization

The corrosion inhibition performance of both unmodified and PEG-modified free fatty acid mixtures was systematically investigated using Tafel polarization measurements in 1 M HCl solution. The polarization curves provide insights into the electrochemical behavior of the A36 carbon steel surface in the presence of different inhibitor systems. Figure 1.3 presents the Tafel polarization plots for tested samples, highlighting the clear shift in corrosion potential (E_{corr}) and significant reduction in corrosion current density (Icorr) upon the addition of both unmodified and PEG-modified inhibitors. These shifts are indicative of suppressed anodic and/or cathodic reactions on the steel surface, resulting in reduced corrosion rates. The extent of this suppression was quantified in terms of inhibition efficiency, calculated from Icorr values, and is analyzed in detail below.

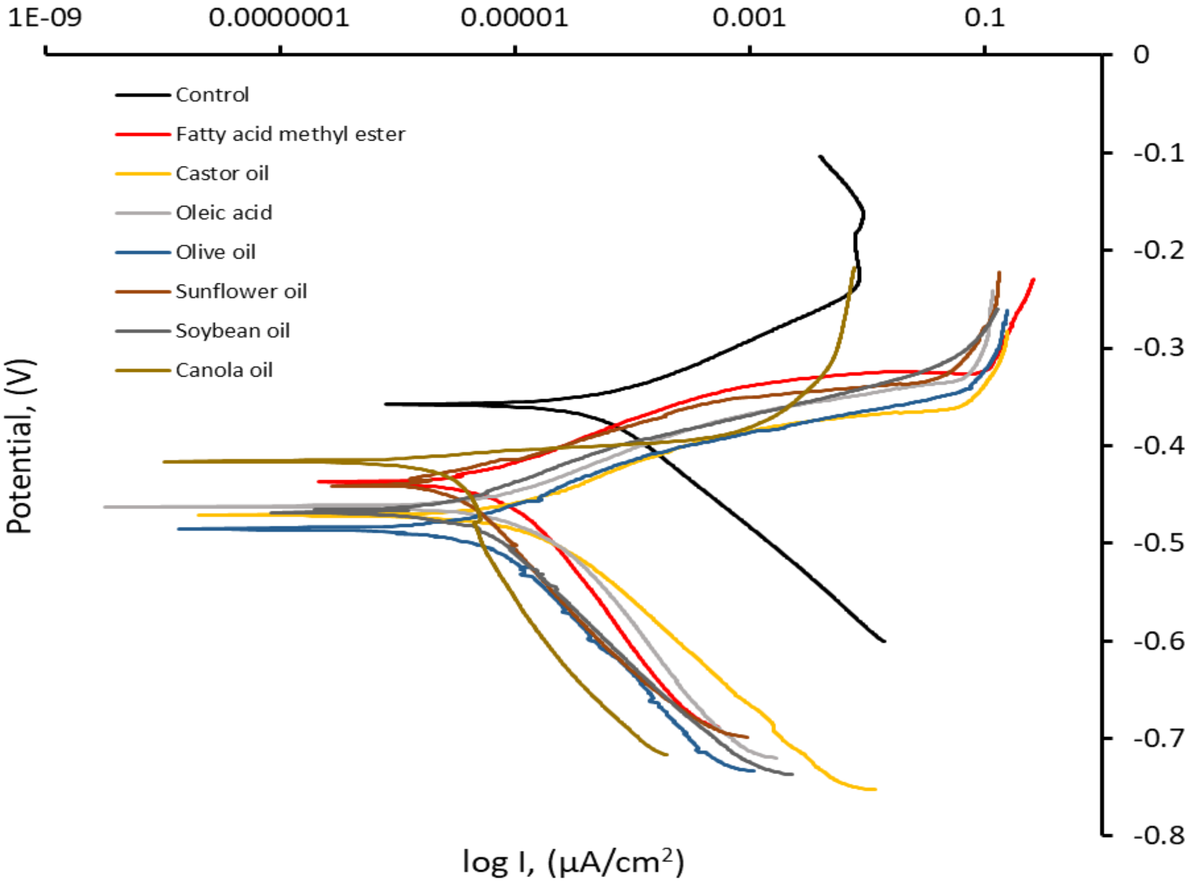

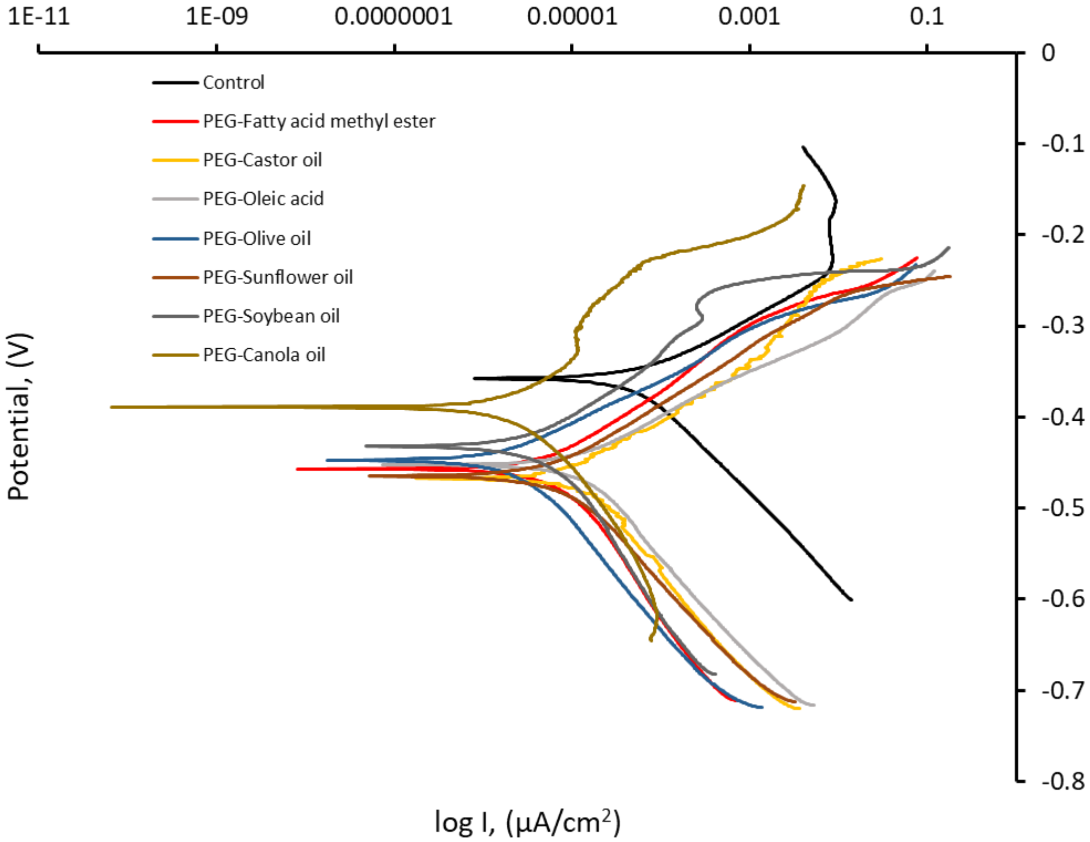

Figure 1.3. Tafel Polarization plots of unmodified (up) and modified free fatty acid mixes (down)

Table 1.4. TAFEL test results of unmodified free fatty acid mixes in 1M HCL and associated inhibition efficiency

Sample	E_{corr} (mV)	Icorr ($\mu A/cm^2$)	CR (mmpy)	Inhibition efficiency (%)
Control	-357	57.1	0.6603	-------
Canola oil	-417.3	9.2	0.1064	83.89
Castor oil	-467.5	14.86	0.1718	73.97
Sunflower oil	-464.6	6.7	0.07748	88.3
Olive oil	-485.3	4.89	0.0565	91.43
Soybean oil	-431.9	6.025	0.06967	89.45
Oleic Acid	-382.3	41.1	0.4753	28.02
Fatty acid methyl ester	-436.7	7.551	0.0873	86.78

Table 1.5. TAFEL test results of modified free fatty acid mixes in 1M HCL and associated inhibition efficiency

Sample	E_{corr} (mV)	Icorr ($\mu A/cm^2$)	CR (mmpy)	Inhibition efficiency (%)
Control	-357	57.1	0.6603	-------
Canola oil	-389.5	2.558	0.02958	95.5

Castor oil	-471.2	11.97	0.1384	79.03
Sunflower oil	-438.5	3.1	0.0358	94.6
Olive oil	-447.3	2.4	0.02775	95.7
Soybean oil	-468.7	4.6	0.0532	91.9
Oleic Acid	-452.75	14.104	0.1631	75.3
Fatty acid methyl ester	-457.2	7.813	0.0903	86.3

The inhibition efficiencies of both unmodified and PEG-modified fatty acid-based inhibitors were evaluated using Tafel polarization data in a 1 M HCl solution (Table 1.4 and 1.5). The control sample, which did not contain any inhibitor, served as the baseline for comparison. Among the unmodified inhibitors, fatty acids derived from olive oil showed the highest inhibition efficiency at 91.43%, followed by soybean oil at 89.45%, sunflower oil at 88.3%, and fatty acid methyl esters (FAME) at 86.78%. Canola oil achieved an efficiency of 83.89%, while castor oil had the lowest efficiency among the natural oils at 73.97%. Pure oleic acid, utilized as a model compound, exhibited a significantly lower efficiency of 28.02%, highlighting the superior performance of natural fatty acid mixtures, likely due to possible synergistic effects.

After modification with PEG (Table 1.5), all inhibitors (excluding FAME) showed a marked improvement in efficiency. Olive oil increased from 91.43% to 95.7%, gaining 4.27 percentage points. Canola oil improved significantly from 83.89% to 95.5%, an increase of 11.61 points. Sunflower oil rose from 88.3% to 94.6%, with an increase of 6.3 points, while soybean oil improved from 89.45% to 91.9%, a rise of 2.45 points. Castor oil increased from 73.97% to 79.03%, showing a gain of 5.06 points. The most notable enhancement was observed in oleic acid, which surged from 28.02% to 75.3%, a remarkable increase of 47.28 points. Conversely, FAME experienced a slight reduction in inhibition efficiency, dropping from 86.78% to 86.3%, a decrease of 0.48 points, suggesting that PEG modification did not further enhance its already high performance.

These quantitative findings confirm that PEG functionalization significantly boosts the corrosion inhibition effectiveness of fatty acid-based inhibitors, particularly for those with initially moderate efficiencies, by improving their solubility, surface activity, and film-forming properties.

3.1.3 Static Weight Loss in 1M HCl

Weight loss measurements were used to evaluate the corrosion inhibition performance of both unmodified and PEG-modified fatty acid-based inhibitors in 1M HCl over a one-week immersion period. The corrosion rate for each inhibitor was compared to that of the control sample (blank, uninhibited 1M HCl solution) to calculate the inhibition efficiency, providing a direct quantitative measure of each inhibitor's protective capability.

Table 1.6. Static weight loss test results of unmodified free fatty acid mixes in 1M HCL and associated inhibition efficiency

Inhibitor	Measured weight	Average	Weight Loss (g)	Corrosion (%)	Inhibitor Efficiency (%)
Control	Weight before corrosion	3.828	-0.526	-13.74%	-
	Weight after corrosion	3.302			
Canola oil	Weight before corrosion	3.796	-0.058	-1.52%	88.96%
	Weight after corrosion	3.739			
Castor oil	Weight before corrosion	3.827	-0.379	-9.91%	27.89%
	Weight after corrosion	3.448			
Sunflower oil	Weight before corrosion	3.835	-0.166	-4.33%	68.49%
	Weight after corrosion	3.669			
Olive oil	Weight before corrosion	3.822	-0.322	-8.42%	38.72%
	Weight after corrosion	3.500			
Soybean oil	Weight before corrosion	3.829	-0.454	-11.86%	13.67%
	Weight after corrosion	3.375			
Oleic Acid	Weight before corrosion	3.812	-0.272	-7.12%	48.16%
	Weight after corrosion	3.541			
Fatty acid methyl ester	Weight before corrosion	3.806	-0.138	-3.63%	73.59%
	Weight after corrosion	3.668			

Table 1.7. Static weight loss test results of modified free fatty acid mixes in 1M HCL and associated inhibition efficeincy

Inhibitor	Measured weight	Average	Weight Loss (g)	Corrosion (%)	Inhibitor Efficiency (%)
Control	Weight before corrosion	3.817	-0.601	-15.74%	-
	Weight after corrosion	3.216			
Canola oil	Weight before corrosion	3.841	-0.037	-0.97%	93.81%
	Weight after corrosion	3.804			
Castor oil	Weight before corrosion	3.802	-0.049	-0.013	91.78%
	Weight after corrosion	3.753			
Sunflower oil	Weight before corrosion	3.826	-0.055	-1.44%	90.88%
	Weight after corrosion	3.771			
Olive oil	Weight before corrosion	3.831	-0.061	-1.59%	89.93%
	Weight after corrosion	3.770			
Soybean oil	Weight before corrosion	3.819	-0.043	-1.12%	92.89%
	Weight after corrosion	3.776			
Oleic Acid	Weight before corrosion	3.772	-0.055	-1.46%	90.69%
	Weight after corrosion	3.717			
Fatty acid methyl ester	Weight before corrosion	3.821	-0.045	-1.19%	92.46%
	Weight after corrosion	3.776			

The results show that all inhibitor systems reduced the corrosion rate of A36 carbon steel to varying degrees, with PEG-modified inhibitors consistently outperforming their unmodified counterparts. Among the unmodified fatty acid inhibitors (Table 1.6), canola oil-derived fatty acids exhibited the highest inhibition efficiency (88.96%), followed by fatty acid methyl ester and those derived from sunflower oil. This trend suggests that the fatty acid composition of each oil source, particularly the degree of unsaturation and chain length, plays a key role in adsorption behavior and protective film formation. Canola oil, which contains a high proportion of oleic acid, likely provides a more uniform and adherent film on the steel surface, leading to better corrosion resistance.

Upon PEG modification (Table 1.7), the inhibition efficiency improved across all oil types. PEG-modified canola oil again demonstrated the most effective inhibition, indicating that the incorporation of polyethylene glycol enhances surface activity and film stability. The amphiphilic nature of the PEG-functionalized molecules likely contributes to stronger interactions with the metal surface and improved dispersion in the aqueous acidic environment, resulting in a more compact and persistent protective layer. PEG-modified soybean and canola oil-based inhibitors also showed marked performance improvements, confirming that the PEGylation step enhances inhibition efficiency regardless of the original oil source.

Overall, the weight loss data confirm the effectiveness of bio-derived inhibitors in reducing steel corrosion under highly acidic conditions. The comparison of inhibitor performance to the control sample revealed significant reductions in mass loss, highlighting the value of PEG modification in boosting inhibitor efficiency. These findings demonstrate that molecular structure, specifically the presence of functional groups like PEG, greatly influences the ability of fatty acid-based inhibitors to form stable, corrosion-resistant films on steel surfaces. The results also support the potential of castor and soybean oil derivatives as leading candidates for environmentally friendly corrosion inhibition in aggressive environments such as 1 M HCl.

Appendix 2
Technical Progress Description for Task 2

Task 2. Simulation-based Inhibitor Implementation Optimization in Gas Gathering and Transportation Pipelines

1. Introduction

1.1 Background

Corrosion inhibitors are widely used in the natural gas pipeline industry to mitigate internal corrosion and extend service life. In practical applications, two primary delivery strategies are commonly employed: batch application, in which inhibitors are introduced intermittently through pigging or slugging operations, and continuous injection, which delivers inhibitors at specific locations along the pipeline. In our ongoing research, we have focused on the latter approach, as it offers a promising route for spatially targeted mitigation, especially in gas pipelines where localized corrosion is often driven by discrete moisture accumulation. Such accumulations commonly occur near geometric irregularities, where water tends to condense and settle, creating high-risk environments that are not easily addressed by global dosing strategies.

In the previous phase of this study, we developed a CFD-based simulation framework to model the long-range transport of inhibitor particles introduced into the gas stream. The goal was to establish a predictive mapping between injection parameters and the resulting deposition patterns along the pipe wall. While this approach proved effective in optimizing global coverage, it was inherently limited in its ability to deliver concentrated protection at localized high-risk regions, where corrosion typically initiates. These limitations highlight the need for a more regionally adaptive injection strategy.

A more efficient approach is to place atomizer-based injection devices near these high-risk regions, enabling direct and localized delivery of inhibitors. However, due to the large spatial extent and structural complexity of pipeline networks, it is impractical to rely on full-domain CFD simulations for each injection scenario. Therefore, in the present study, we construct a short-range inhibitor transport model to simulate particle deposition behavior under a range of representative local conditions. This enables fast and targeted prediction of deposition outcomes for practical use.

To systematize this approach, we propose an integrated corrosion management framework comprising three interconnected components:

(1) High-risk Location Identification, using the Internal Corrosion Direct Assessment (ICDA) methodology to pinpoint regions prone to moisture accumulation and corrosion initiation;

(2) Atomizer Setting Optimization, in which CFD simulation and learning-based models are used to derive efficient injection configurations for targeted protection;

(3) Prediction of Inhibitor Degradation, which accounts for the time-dependent loss of protective effectiveness and informs replenishment planning.

Where the third component was preliminarily addressed in our previous work, where a degradation model was developed to simulate the decline in inhibitor performance over time.

1.2 Objectives

The primary objective of this phase is to construct an integrated framework for risk-guided, localized corrosion inhibitor injection, targeting the most vulnerable segments of gas pipelines. To achieve this, the study is structured around two key components: (1) identifying high-risk locations and (2) optimizing atomizer injection settings for localized protection.

The first component focuses on identifying regions along the pipeline that are especially prone to internal corrosion. To this end, the study implements an ICDA-based assessment using elevation profiles, pressure, and temperature data to evaluate condensation potential and slope-induced fluid retention. A critical slope threshold is applied to identify zones where water accumulation is likely, which are then scored to produce a spatial corrosion risk map.

The second component introduces a short-range particle transport model tailored for inhibitor delivery near these high-risk segments. Unlike previous long-range dispersion models, this approach focuses on localized deposition in common geometric configurations such as elbows and sags. CFD simulations are conducted to evaluate key parameters, including orifice width, particle density, injection rate, and flow velocity, which affect particle-wall deposition behavior. Two typical transport behaviors are observed: 1) Ballistic-like transport, where particles with higher inertia follow parabolic paths and deposit quickly near the injection point; 2) Dispersion-dominated transport, in which smaller particles travel farther with the gas flow and deposit gradually after collision and aggregation. Based on these simulation results, a neural network model is trained to map desired deposition profiles and environmental conditions to the corresponding atomizer settings. The model takes as input the environment parameters and flow information, and outputs optimal injection parameters. This framework enables rapid optimization of injection strategies without requiring new CFD simulations for every condition, thereby supporting practical deployment across complex pipeline networks.

By integrating the three components of our framework containing risk detection, targeted deposition, and time-dependent degradation modeling, this study establishes a structured strategy for corrosion mitigation. This three-step framework, illustrated in Figure 2.1, enables injection resources to be allocated based on actual corrosion risk and pipeline configuration, thereby enhancing both protection efficiency and inhibitor utilization.

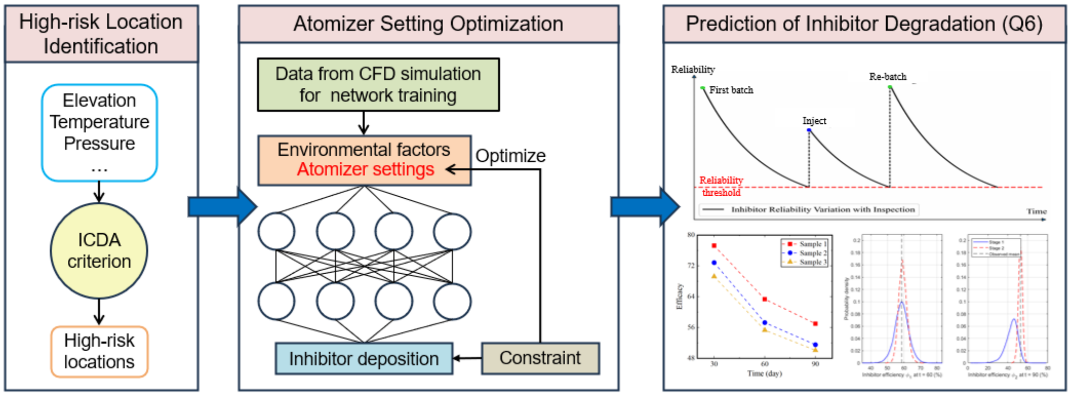

Figure 2.1: Framework of pipeline corrosion protection based on injection application.

2. Methodology

2.1 High-risk location identification based on ICDA

In this study, the identification of high-risk corrosion locations serves as the starting point for region-specific corrosion mitigation. Recognizing that internal corrosion in gas pipelines often originates from water accumulation in geometrically unfavorable regions, such as sags or elbows, this section applies the ICDA methodology to evaluate risk along the pipeline. By integrating topographical and thermodynamic information, the ICDA framework enables the detection of localized condensation zones and stagnant regions that may lead to corrosion initiation. The assessment begins by analyzing the pipeline's elevation profile and computing the temperature and pressure distribution under standard operational conditions. These are used to determine the dew point of the gas phase and identify segments where the local wall temperature falls below this threshold. Additionally, slope analysis is performed to calculate the inclination between adjacent pipe segments. When the slope falls below a critical threshold, fluid retention is more likely to occur, further increasing corrosion risk.

2.1.1 Overview of ICDA-based high-risk location identification

Only limited segments of transmission pipelines—primarily those located in mountainous terrain with lower dew points for water condensation—are at risk for standing water accumulation and the associated threat of internal corrosion. The specific geometric details and layouts of such pipeline segments are often confidential due to safety and commercial concerns. Consequently, identifying these high-risk locations is regarded as a high-value technical challenge, and the use of standard methodologies such as NACE SP0206 and SP0110 is strongly recommended. These standards provide guidelines for determining critical inclination angles and assessing fluid chemistry conditions relevant to internal corrosion under standing water environments. A schematic demonstration of such a high-risk region is illustrated in Figure 2.2, where condensation-induced droplets accumulate in regions with insufficient slope, where condensed liquid may not be effectively drained by gravity. This case visually represents the type of localized geometric configuration in high-risk risk where inhibitors must be strategically applied.

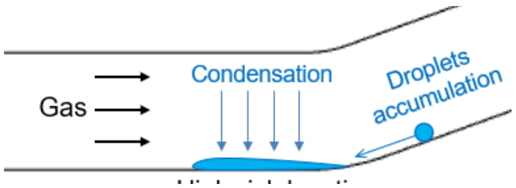

Figure 2.2: Illustration of water accumulation in a low-slope segment of gas pipeline.

To systematically identify such vulnerable regions, we adopt key principles from ICDA to implement a four-step assessment process:

- **Input collection**: essential pipeline properties are collected, including elevation profile, temperature distribution, and operating pressure. Moisture content is recognized as a relevant factor and will be considered in future model refinements as appropriate. The current model primarily focuses on the occurrence of water condensation, which is closely related to moisture content and is a key contributor to corrosion. Further developments may incorporate moisture content more explicitly, depending on the modeling objectives.

- **Dew point and condensation risk estimation**: compute dew point based on environment parameters to identify zones where condensation occurs in a high likelihood.
- **Slope and inclination analysis**: compute the local slope of the pipeline and compare it against an inclination threshold as suggested by industry experience and ICDA standards. Segments below this threshold are flagged as prone to liquid retention.
- **Risk scoring and visualization**: Integrate condensation risk and slope flatness to produce a composite risk score. This enables the generation of a spatial risk map to prioritize inhibitor injections at key locations.

2.1.2 Numerical implementation of ICDA-based risk identification

To illustrate the ICDA-based risk identification procedure, a representative pipeline segment was constructed under synthetic conditions. While not intended to reflect a specific real-world case, this example serves to demonstrate the computational process and the integration of thermodynamic and geometric considerations.

Table 1 summarizes the input parameters, including the initial gas temperature and pressure, soil temperature, and heat transfer coefficient. A 2000-meter pipeline is discretized into 300 segments, and the elevation profile is generated by superimposing sinusoidal functions with smoothed white noise, simulating topographic variation. The gas temperature along the pipeline is updated iteratively using a simple heat exchange model:

$$T_i = T_i - K \cdot (T_{i-1} - T_s) \cdot \Delta x \tag{2.1}$$

where the Heat transfer coefficient K is set as 0.001. The dew point temperature T_{dew} is estimated empirically as a linear function of local gas pressure, following field-derived correlations:

$$T_{dew} = 10 + 0.4 \cdot (P - 30) \tag{2.2}$$

where the Operating pressure P is modeled as a function of elevation, assuming greater elevation leads to higher frictional losses:

$$P(x) = P_0 - \frac{(h(x) - h_{min})}{200} \tag{2.3}$$

where $h(x)$ denotes the elevation at distance x and h_{min} is the minimum elevation. As shown in Figure 2.3, condensation risk is identified in regions where the gas temperature drops below the dew point. These segments are preliminarily flagged as potential liquid formation zones.

Table 1. Simulation parameters for ICDA-based pipeline condition modeling.

Parameter	Value
Number of discrete points	300
Distance x	0 - 2000 m
Initial temperature T_0	30 °C

Initial pressure P_0	50 bar
Soil temperature T_s	10 °C
Heat Transfer Coefficient K	0.001

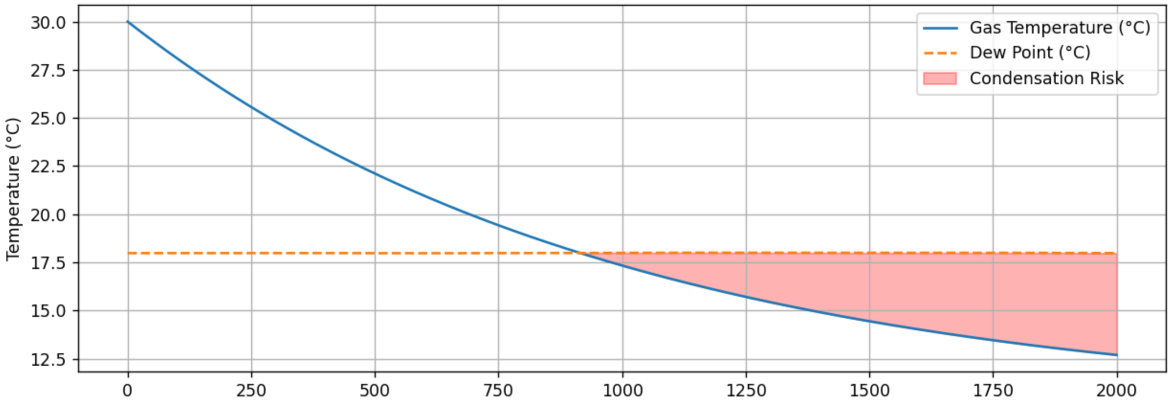

Figure 2.3: Gas temperature and dew point distribution along pipeline.

Subsequently, local slopes are computed from the elevation profile. As illustrated in Figure 2.4, segments with slopes below a critical threshold (taken here as 0.3°) are flagged as prone to water retention. Red markers indicate locations where both condensation and low-slope conditions are met, representing potential high-risk zones for internal corrosion. This outcome serves as a starting point for subsequent injection optimization in the overall framework.

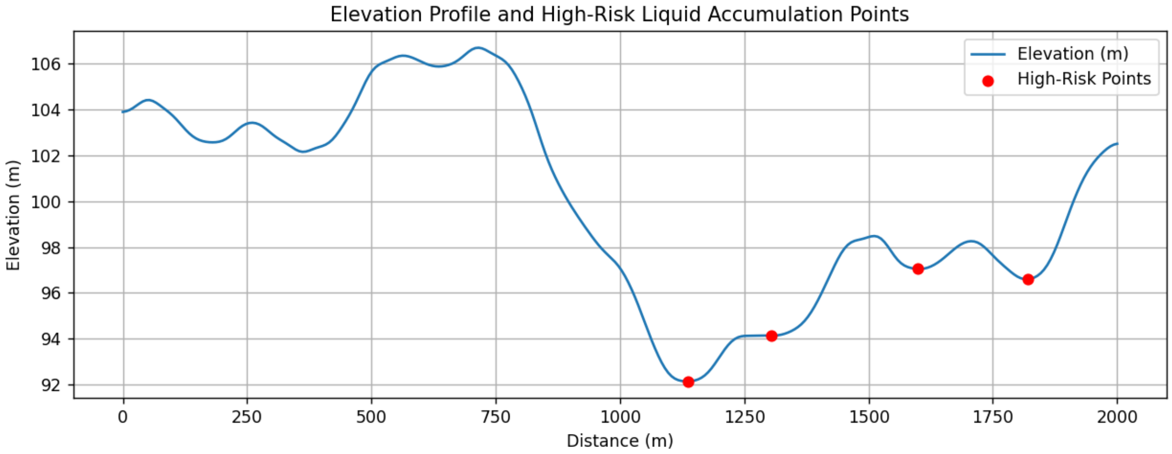

Figure 2.4: Elevation profile and high-risk water accumulation points.

2.2 AI-enhanced prediction of optimal atomizer settings

2.2.1 Effect of CFD parameters on particle transport

To enable the development of an Injection Control Network (ICN) for optimal atomizer setting prediction, it is essential to first understand the short-range transport mechanisms of inhibitor particles and identify the dominant influencing factors. Unlike long-distance transport dominated by fluid-phase advection, localized injection presents a distinct balance between gravitational settling and flow-induced drag. The gravitational force acting on an individual particle is governed by:

$$F_g = \frac{1}{6}\pi\rho_p d_p^3 g \tag{2.4}$$

where ρ_p is the particle density, d_p is the particle diameter, and $g = 9.81m \cdot s^2$ denotes the gravitational acceleration. The density and diameter directly affect the particle's weight and settling tendency, while the flow velocity contributes to drag force and controls the horizontal transport distance before deposition occurs. Among these, flow velocity is considered an environmental constraint, typically fixed by pipeline operation. In contrast, particle diameter and density are controllable through the design of injection settings, particularly the orifice width and injection speed, which influence droplet breakup and atomization characteristics. These controllable parameters are therefore the primary focus in optimizing atomizer configurations.

It is important to note that gravitational force is only one of several forces acting on an injected particle. In addition to drag, which dominates forward transport, particles also experience lift forces due to velocity gradients and flow separation, especially near boundary layers. As particle size decreases, the influence of gravity diminishes relative to these fluid-mediated forces. This effect is particularly pronounced for small particles, whose motion can become highly sensitive to turbulent fluctuations or streamline distortion. As illustrated in Figure 2.5, particles with identical density but smaller diameters, such as those around 1×10^{-4} m, exhibit significant deviation from idealized ballistic trajectories. Their paths are increasingly influenced by local fluid disturbances, resulting in irregular or dispersed motion. This transition from gravity-dominated ballistic transport to flow-coupled dispersion highlights the need for careful parameter control in atomizer design, particularly when targeting precise deposition patterns.

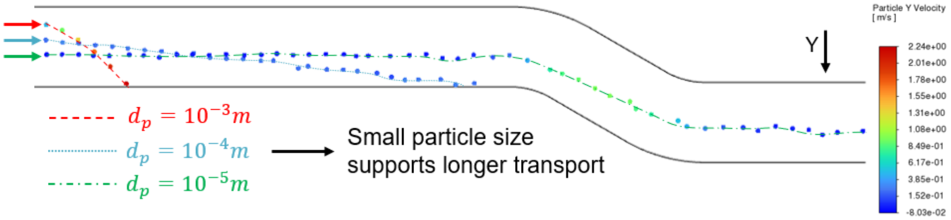

Figure 2.5: Transport behavior of particles with different magnitudes of diameters.

To explore the impact on deposition behavior, we present and analyze particle distributions and deposition profiles for several CFD cases with orifice widths of 6×10^{-4} m, 5×10^{-4} m, 4×10^{-4} m and 3×10^{-4} m when the particle density is 1100kg/m^3, respectively. Each case is supported by the spatial distribution of particles within the pipe and wall-deposition amount.

To explore the impact on deposition behavior, we present and analyze particle distributions and deposition profiles for several CFD cases with orifice widths, which determines the initial particle diameter via atomization behavior, as shown in Figure 2.6. To better capture realistic particle evolution, the discrete phase model includes coalescence and breakup interactions, enabling a more accurate representation of particle size dynamics during injection and transport.

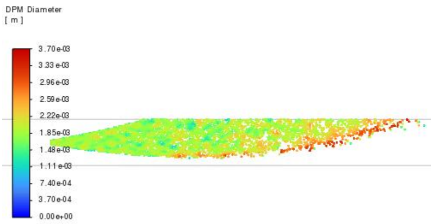

(a) orifice width = 6×10⁻⁴ m.

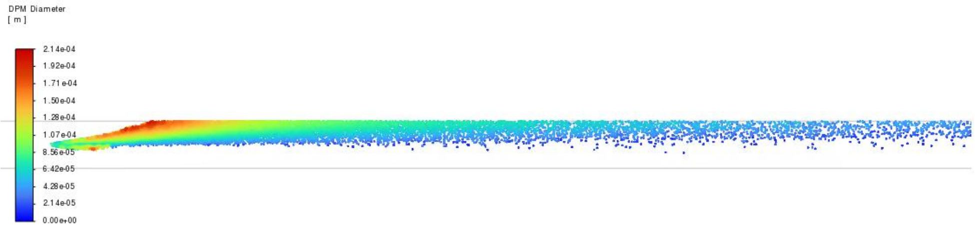

(b) orifice width = 5×10⁻⁴ m.

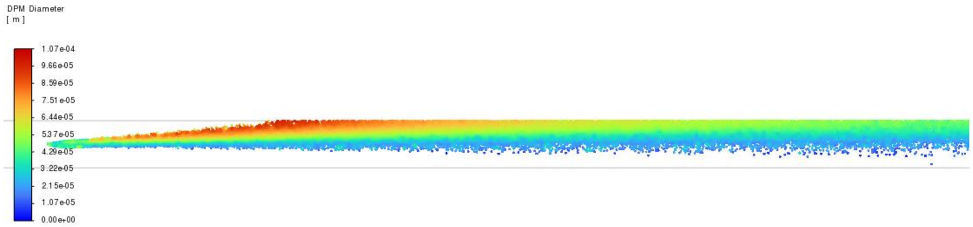

(c) orifice width = 4×10⁻⁴ m.

Figure 2.6: Particle transport behavior under different orifice widths.

The result in Figure 2.6 (a) with an orifice width of 6×10^{-4} m exhibits particle diameters mostly around the order of 10^{-3} m, leading to rapid settling due to strong gravitational influence. The particles follow ballistic trajectories, resembling projectile motion, and deposit over a short horizontal distance. This regime is therefore referred to as ballistic transport. In contrast, results from Figure 2.6 (b) and Figure 2.6 (c), with narrower orifices of 5×10^{-4} m and 4×10^{-4} m, generate particles primarily below 10^{-4} m in diameter. These smaller particles exhibit lower settling velocities and are more strongly influenced by the surrounding fluid flow, resulting in broader axial dispersion and delayed deposition. This behavior corresponds to a dispersion-dominated regime, where drag forces outweigh gravitational effects.

Figure 2.7 further presents the evolution of wall deposition profiles under varying orifice widths, further illustrating the gradual shift in transport regime from dispersion-dominated to ballistic behavior. In this demonstration, a comparison between orifice widths just below and above the transition threshold reveals the shift in deposition behavior more clearly. For orifice widths below 5.4×10^{-4} m, the deposition curves resemble right-skewed F-distributions with long tails, reflecting dispersion-dominated transport. As the orifice widens, particle size increases, leading to shorter transport distances and a higher accumulation of deposited particles within the computational domain. At 5.4×10⁻⁴ m, the system enters a transitional regime. The deposition peak becomes more pronounced, but its shape also begins to distort. This marks the onset of ballistic-dominated transport, where heavier particles settle more quickly. Beyond 5.6×10⁻⁴ m, the deposition profile adopts a steep-front, flat-decay pattern. The peak position stabilizes spatially, but its magnitude decreases due to a broader frontal dispersion. This shape is characteristic of ballistic transport, where gravity rapidly dominates particle motion, producing a plateau-like decline rather than a long tail.

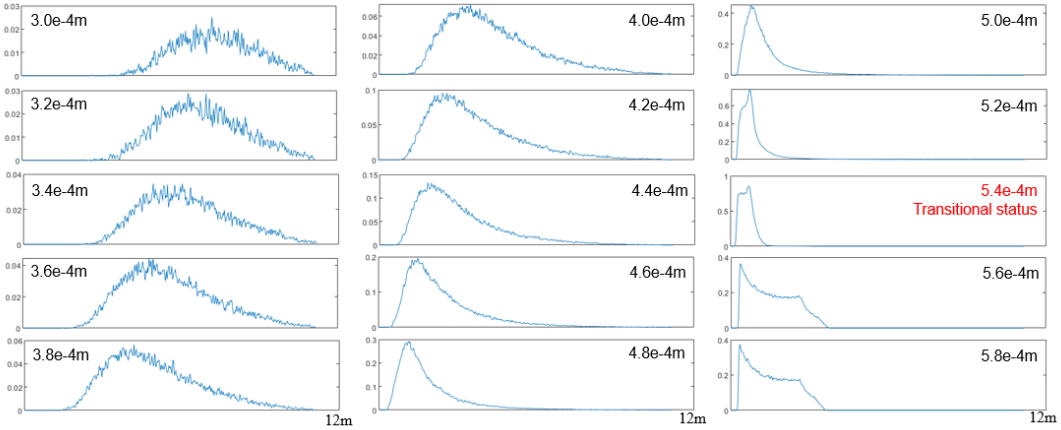

Figure 2.7: Evolution of particle deposition under different orifice widths.

Understanding the underlying particle transport regimes helps to anticipate deposition patterns under different injection parameters and thus informs the optimization strategy. For example, based on the above demonstration, orifice widths greater than 5.2×10⁻⁴ m can be used as a threshold to ensure that particles enter either the transitional or ballistic regime, thereby promoting more concentrated and efficient deposition near the targeted region.

2.2.2 Training of Injection Control Network to optimize atomizer setting

To efficiently determine optimal atomizer settings for targeted particle deposition, an Injection Control Network (ICN) is constructed and trained based on CFD-derived data. The overall learning-based optimization framework is illustrated in Figure 2.8. The ICN first learns a forward mapping from a given combination of injection parameters and environmental conditions to the resulting deposition distribution. Once trained, the model is used inversely: instead of prescribing an entire deposition profile, only selected output locations are constrained to meet engineering requirements typically by enforcing that deposition values exceed a predefined threshold. This targeted constraint is then used to guide gradient-based backpropagation through the ICN, while also respecting bounds or feasibility constraints on the atomizer input parameters, enabling inverse optimization of spray settings.

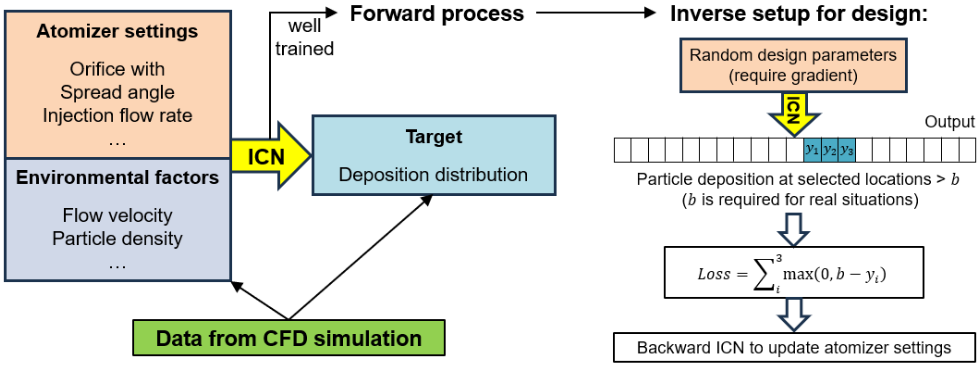

Figure 2.8: Problem description of optimal atomizer setting with Injection Control Network.

While the design framework incorporates multiple parameters—including injection rate, particle density, orifice height, and spray angle—this study focuses on a minimal and representative subset to demonstrate the feasibility of the approach. As shown in Figure 2.9, the ICN model inputs include injection spread angle a_s, orifice width w and flow velocity v_f. The output is the Fourier spectrum of the deposition profile at each spatial location, capturing both amplitude and phase information via real and imaginary parts. This spectral representation reduces spatial sensitivity and facilitates smoother optimization during backpropagation. Importantly, injection time is not explicitly considered as a network input. As demonstrated in Figure 2.10 (bottom middle), deposition magnitude increases approximately proportionally with time, preserving the spatial profile shape. This allows time-based scaling to be applied externally during inference, significantly simplifying model complexity.

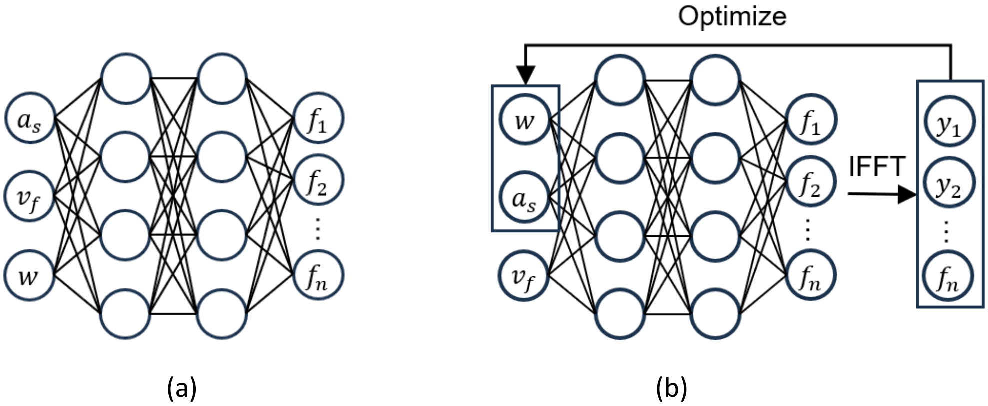

Figure 2.9: Illustration of ICN architecture at (a) forward inference and (b) backward optimization.

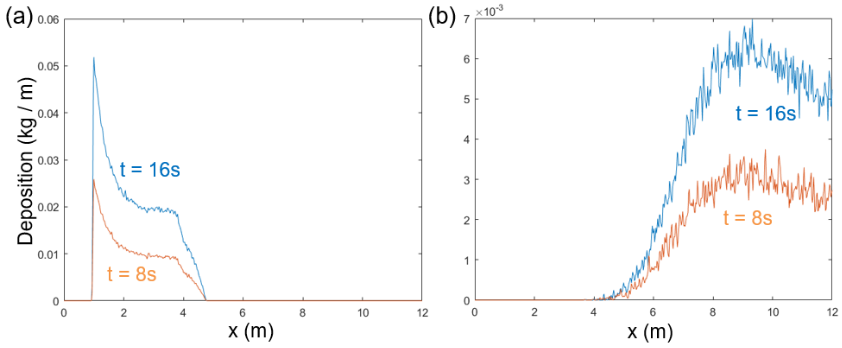

Figure 2.10: Demonstration of proportional scaling in deposition magnitude with time in cases of (a) the ballistic transport and (b) the dispersion transport.

To train the ICN, a dataset is generated by sampling across three selected parameters, where $a_s \in \{20°, 25°, 30°\}$, $w \in [3 \times 10^{-4}, 6 \times 10^{-4}]$ m (15 uniform intervals) and $v_f \in [1.0, 2.0]$ m/s (10 uniform intervals). Testing samples are randomly selected within the same parameter ranges to validate the model's generalization ability, as shown in Figure 2.11.

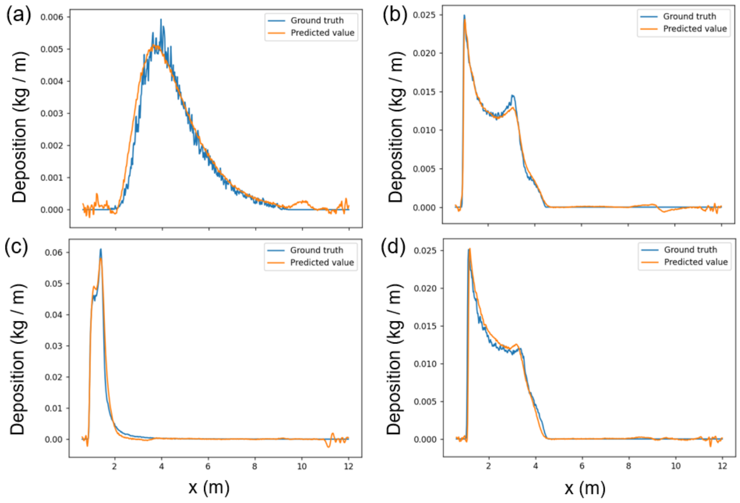

Figure 2.11: Testing results of the well-trained ICN under different input parameters with (a) $a_s = 25.3080$, $w = 3.1619 \times 10^{-4}$ and $v_f = 1.0759$, (b) $a_s = 20.0463$, $w = 5.8857 \times 10^{-4}$ and $v_f = 1.1067$, (c) $a_s = 25.1325$, $w = 4.0529 \times 10^{-4}$ and $v_f = 1.6221$ and (d) $a_s = 28.6869$, $w = 5.4519 \times 10^{-4}$ and $v_f = 1.7749$.

Once the ICN is trained, it enables inverse optimization by adjusting input parameters to achieve desired deposition characteristics. For illustration, we assume that particle accumulation should exceed 0.05 kg/m in a localized region $x \in [2, 3]$. Multiple combinations of atomizer settings may satisfy this condition. To guide the optimization toward practically desirable solutions, additional input-side constraints can be incorporated into the loss function.

In Example 1, a preference for dispersion-dominated transport is enforced by referencing the response surface shown in Figure 2.12. Based on the identified regime boundary between dispersion and ballistic behavior, additional condition $w > 4.5 \times 10^{-4}$ is set to encourage the optimizer to favor dispersion-dominated transport regimes. In this cases, the loss function with a regularization term is written as:

$$Loss = \sum \mathrm{ReLU}(0.05 - y_i) + \mathrm{ReLU}(4.5 \times 10^{-7} - w) \tag{2.5}$$

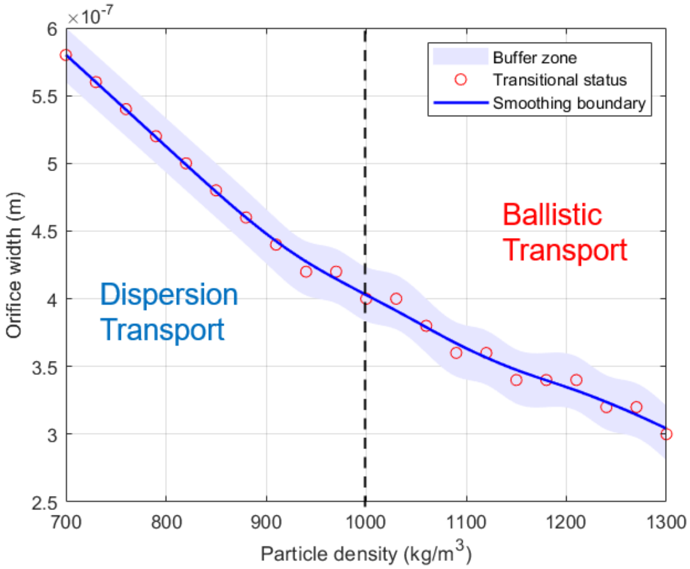

Figure 2.12: Testing results of the well-trained ICN under different input parameters with

In Example 2, a design constraint on the maximum spread angle is introduced by limiting the injection angle to $a_s > 20°$, which may arise due to structural or manufacturing limitations. Correspondingly, the loss function is written as:

$$Loss = \sum \mathrm{ReLU}(0.05 - y_i) + \mathrm{ReLU}(25 - a_s) \tag{2.6}$$

These added constraints reshape the feasible design space and shift the optimizer toward solutions that align with engineering realities.

The above flexible formulation allows ICN-based optimization to account not only for output accuracy but also for operational preferences and physical feasibility—enabling practical deployment in real-world design scenarios.

3. Future research

While the current phase has successfully developed a predictive framework for inhibitor transport and deposition, the lack of field validation and the limited understanding of how deposition patterns translate to actual protective performance remain critical limitations. The next phase of research will therefore shift focus toward experimental measurement, data-driven assessment, and risk quantification.

Based on the discussion and comments from TAP members, two potential directions have emerged from the initial analysis and discussions. One involves the development of methods, for characterizing key properties of the inhibitor film, such as thickness, distribution, and coverage. The other focuses on simulating direct injection method for long distance travel and water-soluble inhibitor in gathering pipelines. These two directions may serve as complementary paths to strengthen the link between model predictions and real-world corrosion risk, depending on feasibility and industry relevance.

In parallel, AI-assisted image recognition techniques are considered as a means to automate the detection and classification of inhibitor film coverage and localized corrosion features. If validated, these algorithms could enable fast and consistent analysis, both in laboratory settings and potentially in field applications.

Additionally, the construction of a multi-factor corrosion safety index is under preliminary discussion, which would aim to integrate measurement data, model outputs, and operational parameters into a unified risk framework. This could lay the groundwork for a lightweight decision-support tool, enabling engineers to better assess corrosion risks and adapt injection strategies accordingly.

These proposed efforts, if pursued, would help bridge the gap between computational modeling and field implementation, improving both the diagnostic accuracy and practical applicability of inhibitor optimization strategies in complex pipeline systems.

References

1. Al-Moubaraki, A. H., and I. B. Obot, Top of the line corrosion: causes, mechanisms, and mitigation using corrosion inhibitors. Arabian Journal of Chemistry, 2021. 14(5): p. 103116.

2. Jayaweera C D, Fernandes del Pozo D, Hitsov I P, et al. Assessing the feasibility of using a data-driven corrosion rate model for optimizing dosages of corrosion inhibitors[J]. npj Materials Degradation, 2024, 8(1): 127.